

Supplementary Appendix for *Mechanics unlocks the morphogenetic puzzle of interlocking bivalved shells*

Derek E. Moulton^a, Alain Goriely^a, and Régis Chirat^b

^aMathematical Institute, University of Oxford, Oxford, OX2 6GG, UK; ^bCNRS 5276, LGL-TPE, Université Lyon 1, 69622 Villeurbanne Cedex, France

1. Base shell geometry

In this section we present a geometrical construction for the base bivalved shell, i.e. the shape without any ornamentation. We suppose that the initial shell edge is given parametrically by the planar curve

$$\mathbf{r}_0 = \mathbf{r}(s, 0) = (x_0(s), y_0(s), 0), \quad [1]$$

where s is assumed an arclength parameterisation for the initial curve. Following (1), the surface of the shell is generated by evolving the initial curve $\mathbf{r}(s, 0)$ via an imposed vector field that represents the growth velocity at each point. As shown in (1), the growth can be more intuitively understood by working in a local coordinate basis attached to the shell curve itself, and moreover a self-similar shape of the shell may be easily generated through simple local rules for the local growth velocities. We define the local coordinate basis $\{\mathbf{d}_i\}$, $i = 1, 2, 3$, such that \mathbf{d}_3 aligns with the tangent to the curve, thus satisfying $\mathbf{r}'(s, t) = \lambda(t)\mathbf{d}_3$ where λ characterises the stretch of the base curve and prime denotes differentiation with respect to s . The basis vector \mathbf{d}_1 is chosen to be the unit normal vector, and $\mathbf{d}_2 = \mathbf{d}_3 \times \mathbf{d}_1$ is the binormal vector. We also define the two axial vectors \mathbf{u} and \mathbf{w} , which satisfy (overdot denotes time derivative):

$$\mathbf{d}'_i(s, t) = \mathbf{u} \times \mathbf{d}_i, \quad \dot{\mathbf{d}}_i(s, t) = \mathbf{w} \times \mathbf{d}_i \quad [2]$$

The growth velocity is expressed by writing

$$\dot{\mathbf{r}}(s, t) = \sum_{i=1}^3 q_i \mathbf{d}_i, \quad [3]$$

where the local velocity field $\{q_1, q_2, q_3\}$ governs the evolution of the base curve and thus generates the surface of the shell. To generate a bivalved shell, it suffices to combine a coiling growth with a radial dilation. This is expressed as

$$\begin{aligned} q_1 &= \mathbf{c}\mathbf{r}_0 \cdot \mathbf{d}_1(s, 0), \\ q_3 &= \mathbf{c}\mathbf{r}_0 \cdot \mathbf{d}_3(s, 0), \\ q_2 &= bx_0(s). \end{aligned} \quad [4]$$

The components q_1 and q_3 expand the curve without changing the shape, i.e. dilation, while the component q_2 generates coiling via the linear gradient of growth, taken without loss of generality to coincide with the x -axis of the initial curve, in the binormal direction. Note that $q_2 = 0$ at points initially along the y -axis – this axis thus serves as a hinge about which the valve rotates in order to close or open.

From the prescribed velocity field, the shell surface is computed by solving for the stretch factor λ and the axial vectors \mathbf{u}, \mathbf{w} via the system of equations obtained by imposing that time and space derivatives commute:

$$\begin{aligned} (\dot{\mathbf{r}})' &= (\mathbf{r}')', \\ (\dot{\mathbf{d}}_i)' &= (\mathbf{d}_i)', \quad i = 1, 2, 3 \end{aligned} \quad [5]$$

and casting these equations into the local basis (for more details see (1)). Key to this form of velocity field is that the curve remains planar and the curvature does not vary with time, that is $\mathbf{u} = u_2(s)\mathbf{d}_2$, where $u_2(s)$ is the curvature of the base curve, while the stretch λ has the simple form $\lambda = 1 + t$. Analytical forms for \mathbf{w} can also be determined :

$$w_1 = \frac{-bx'_0(s)}{1+t}, \quad w_2 = 0, \quad w_3 = \frac{-by'_0(s)}{1+t}. \quad [6]$$

With \mathbf{w} known, the full surface of the shell is obtained by integrating the system of equations

$$\dot{\mathbf{d}}_i = \mathbf{w} \times \mathbf{d}_i, \quad \dot{\mathbf{r}} = \sum_{i=1}^3 q_i \mathbf{d}_i. \quad [7]$$

Due to the form of time dependence in the axial vector \mathbf{w} , an explicit solution for Eq. (7) can be attained. In particular, writing $\dot{\mathbf{d}}_i = \mathbf{w} \times \mathbf{d}_i$ in matrix form $\dot{\mathbf{D}} = \mathbf{D}\mathbf{W}$, where the columns of \mathbf{D} are the basis vectors \mathbf{d}_i and \mathbf{W} is a skew symmetric matrix comprised of the components of \mathbf{w} , we can solve exactly to obtain

$$\mathbf{D} = \mathbf{D}_0 \left(\mathbf{1} + \frac{\lambda}{b} \mathbf{W} \sin(b \ln \lambda) + \frac{\lambda^2}{b^2} \mathbf{W}^2 (1 - \cos(b \ln \lambda)) \right),$$

where $\mathbf{D}_0 = \mathbf{D}_0(s)$ gives the basis at $t = 0$ and $\mathbf{1}$ is the identity matrix. The full surface is then obtained by integrating $\dot{\mathbf{r}} = \mathbf{D}\mathbf{q}$, yielding the explicit formula

$$\begin{aligned} \mathbf{r} = \mathbf{r}_0 + \mathbf{D}_0 \left(\mathbf{1} + \frac{\lambda^2}{b^2} \mathbf{W}^2 \right) \mathbf{q} t + \frac{\lambda}{b(1+b^2)} \mathbf{D}_0 \mathbf{W} \mathbf{q} (\lambda \sin(b \ln \lambda) - b \lambda \cos(b \ln \lambda) + b) \dots \\ \dots - \frac{\lambda^2}{b^2(1+b^2)} \mathbf{D}_0 \mathbf{W}^2 \mathbf{q} (\lambda \cos(b \ln \lambda) + b \lambda \sin(b \ln \lambda) - 1). \end{aligned} \quad [8]$$

This construction is repeated for both valves of the shell. As we have set $c = 1$ for both valves, the coiling rate need not be the same for the two valves; so long as the initial curves and dilation rates match, the shell edge of each valve will be the same at all times. To generate two opposing valves, either the coiling is inverted for one valve, i.e. we send $b \rightarrow -b$, or we simply reflect the surface constructed above about the $z = 0$ plane. For the two valves to be in a closed state also requires each valve to rotate about its hinge such that the shell edge lies in the $z = 0$ plane. In the formulation with constant b , the necessary angle of rotation is easily worked out to be $b \ln(1+t)$.

2. Plane of ornamentation

In this section we derive the plane of ornamentation, based on the argument of the main text that the generative zone strain should be balanced by points deforming ‘up’ and ‘down’. As a starting point we suppose that the base shell has been constructed as in Section 1, and is given parametrically by $\mathbf{r}(s, t)$.

We define the ‘true antimarginal’ plane as the plane spanned by the tangent direction along the shell edge in the *material* s -direction – the basis vector \mathbf{d}_3 – and the direction orthogonal to both \mathbf{d}_3 and the tangent to the shell edge in the *growth* direction t ; the latter can be computed as the vector

$$\mathbf{v} = \frac{\dot{\mathbf{r}}}{|\dot{\mathbf{r}}|} \times \mathbf{d}_3 = \frac{q_2 \mathbf{d}_1 - q_1 \mathbf{d}_2}{\sqrt{q_1^2 + q_2^2}}. \quad [9]$$

We consider rotating this plane about the tangent to the shell edge, the \mathbf{d}_3 direction, by angle θ . Defining this rotated direction by $\hat{\mathbf{v}}$, we have

$$\hat{\mathbf{v}} = \frac{(\cos \theta q_2 + \sin \theta q_1) \mathbf{d}_1 + (\sin \theta q_2 - \cos \theta q_1) \mathbf{d}_2}{\sqrt{q_1^2 + q_2^2}}. \quad [10]$$

The angle of rotation $\theta = \theta(s, t)$ is determined based on the following idea: through ornamentation, the mantle (and thus the shell edge) will deform ‘up’, which we may denote by the $\hat{\mathbf{v}}$ direction, as well as ‘down’, the $-\hat{\mathbf{v}}$ direction. This deformation will change the total shell arclength in the growth (t) direction, which is proportional to the length of the generative zone, i.e. the amount of shell length being added through secretion. This change in arclength will moreover occur by unequal amounts at the ‘up’ and ‘down’ points. However, there should be no such difference in arclength (at least locally), as the shell arclength in the t direction is a feature of the base coiling rate. The differential in arclength will thus generate a strain in the generative zone: the generative zone will be in tension where the arclength increases and in compression where it decreases. This differential strain will generate a moment in the shell-secreting mantle edge, serving to rotate the plane of ornamentation until the arclength at the maximally up point is equal to that at the maximally down point.

Computationally, we define

$$\begin{aligned} \mathbf{r}_{\text{up}} &= \mathbf{r} + \epsilon \lambda \hat{\mathbf{v}} \\ \mathbf{r}_{\text{down}} &= \mathbf{r} - \epsilon \lambda \hat{\mathbf{v}}. \end{aligned} \quad [11]$$

Here ϵ is a small constant that characterises the amplitude of deflection of the mantle at the point of buckling (as we show this term drops out of the computation), and the scale factor $\lambda = \lambda(t)$ characterises the amplification of the buckling pattern during development as discussed in the main text. The condition for the angle θ is that the arclengths at the ‘up’ and ‘down’ points are equivalent at all times, which will hold if and only if

$$\|\dot{\mathbf{r}}_{\text{up}}\| = \|\dot{\mathbf{r}}_{\text{down}}\|. \quad [12]$$

Expanding the norm and simplifying, we obtain the following differential equation

$$\dot{\mathbf{r}} \cdot (\dot{\lambda} \hat{\mathbf{v}} + \lambda \dot{\hat{\mathbf{v}}}) = 0. \quad [13]$$

Since λ and \mathbf{r} are known, and $\hat{\mathbf{v}}$ is defined in terms of θ , Eq. (13) provides a nonlinear differential equation in t for θ at each point s . Since the two valves of the shell are curves in the same plane at $t = 0$, we give the initial condition $\theta(s, 0) = 0$.

Once θ is computed, which we have done numerically, we can quantify the degree of alignment of the plane of ornamentation in a simple way. As stated, the two valves are closed by rotating the shells about the y -axis such that the shell edge lies in the $z = 0$ plane. The angle of rotation is $\varphi = \varphi(t) = b \ln(1 + t)$ as stated above for constant coiling b . Since the rotated shell has the shell edge always in the x - y plane, the two valves have perfectly coinciding planes of ornamentation if the rotated shell has the property that $\hat{\mathbf{v}}$ is aligned with \mathbf{e}_z .

We thus define the alignment measure

$$\mathcal{A}(s, t) = R(\varphi, \mathbf{e}_y) \hat{\mathbf{v}} \cdot \mathbf{e}_z,$$

where $R(\varphi, \mathbf{e}_y)$ is the rotation matrix that places the shell edge in the x - y plane at all times and $\hat{\mathbf{v}}(s, t)$ satisfies Eq. (10), Eq. (13). The quantity \mathcal{A} should be equal to one for any points where the plane is in perfect alignment. In Fig 1, we plot $\mathcal{A}(s, t)$ as a surface for different coiling rates. We find near perfect alignment save for a small transition region near $t = 0$ (likely due to the imperfect condition of having to provide a finite curve at $t = 0$).

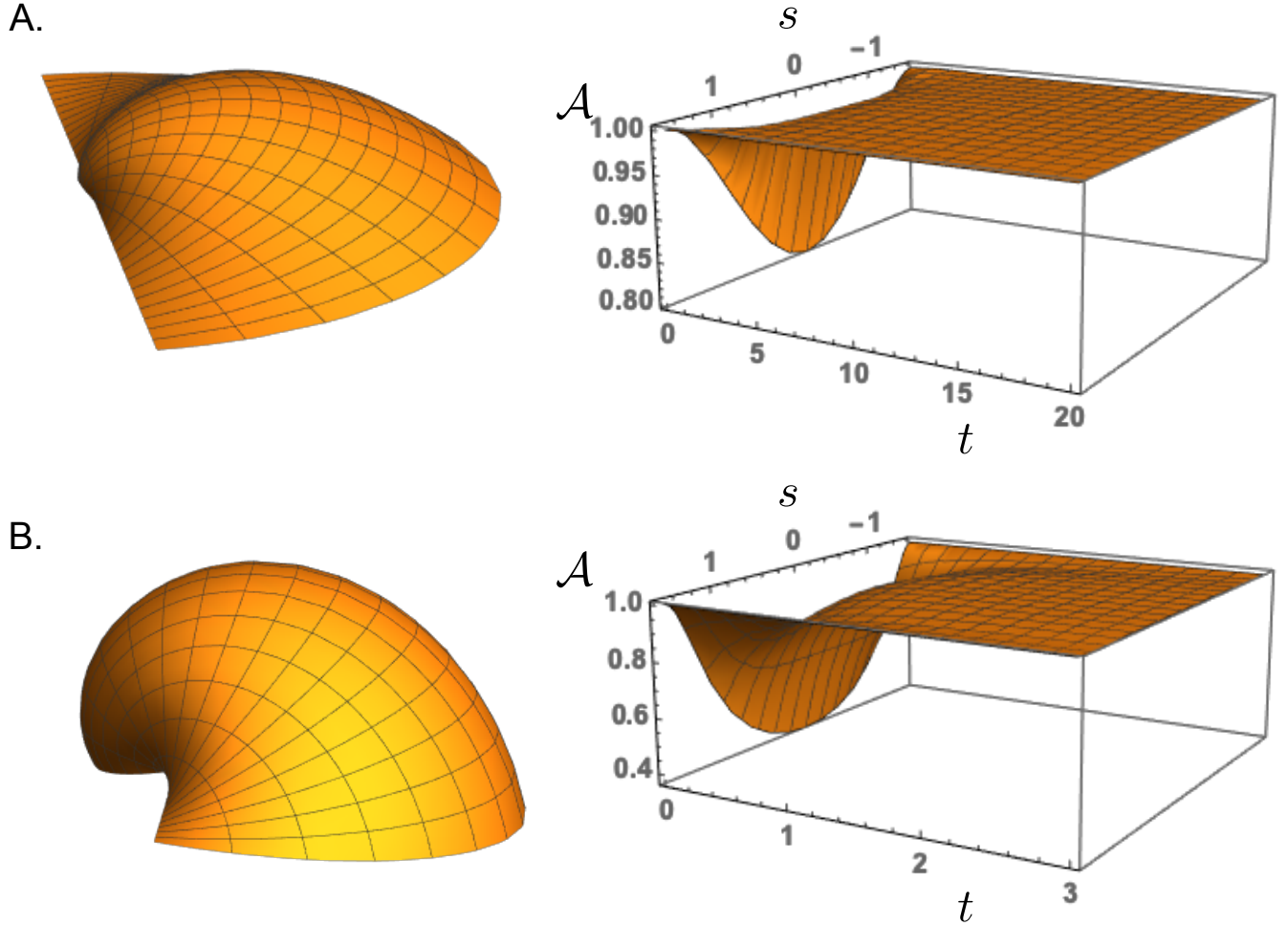


Fig. 1. Alignment measure of plane of ornamentation for a shell with low coiling rate (A) and a shell with high coiling rate (B). The simulated shells prior to small-scale ornamentation are shown at left, the surface of alignment measure \mathcal{A} is shown at right. Perfect alignment corresponds to $\mathcal{A} = 1$, which is attained for nearly all points in time and space.

3. Ornamentation as mechanical instability

In this section we outline the computation for mechanical instability that produces the small-scale ornamentation pattern. As described in the main text, we consider the two mantle edges as growing planar inextensible elastic rods. In this setting, the mantle edge is described by a curve $\mathbf{r}(s) = (x(s), y(s))$ satisfying the geometric relation

$$x'(s) = \gamma \cos \theta(s), \quad y'(s) = \gamma \sin \theta(s), \quad [14]$$

where $\theta(s)$ is the angle between the tangent to the curve and the x -axis, and γ characterises growth via an increase in reference arclength. Here s is an initial Lagrangian arclength parameter for the material before any growth (equivalent to the geometric parameter s). Letting $\mathbf{n} = (n_x(s), n_y(s))$ denote the resultant force in the elastic material, and $m(s)$ the resultant moment, balance of linear and angular momentum read

$$\mathbf{n}'(s) + \mathbf{f} = 0, \quad m'(s) = \gamma n_x \sin \theta - \gamma n_y \cos \theta, \quad [15]$$

where \mathbf{f} is the force applied to the mantle by attachment to the calcified shell edge (and any external forces). In the simplest version of attachment to a flat shell providing linear resistance to deformation in the y -direction, we would have $\mathbf{f} = -kE_b y(s)\mathbf{e}_y$, where k characterises the strength of attachment relative to bending stiffness. The system is completed with a constitutive law for the moment and boundary conditions. For the former, we take the standard linear relation $m(s) = E_b \theta'(s)/\gamma$, the division by γ appearing due to the choice of working in the Lagrangian arclength.

The best choice of boundary conditions at the ends of the shell edge is not entirely clear, but either clamped or pinned are reasonable choices, and the choice of one over the other will not change the basic result. Results in this paper have been plotted for clamped boundaries.

For deformation of the two mantle edges in a growing bivalved shell, we must solve two copies of the system, one for the mantle edge of each valve, and with an added repulsive interaction force that ensures that the two mantles cannot interpenetrate. That is, we must simultaneously solve Eq. (14), Eq. (15) for both mantle edges, with an additional term in \mathbf{f} that accounts for the interaction of the two mantles. Letting δ denote the half-width of each mantle, L the length of the domain, and using subscript $i = 1, 2$ for the two respective mantles, the clamped boundary conditions read:

$$y_1(0) = y_1(L) = \delta, \quad y_2(0) = y_2(L) = -\delta, \quad \theta_i(0) = \theta_i(L) = 0, \quad i = 1, 2.$$

To derive the repulsive interaction force of the two mantles, we begin with an energy potential that diverges when the two centerlines overlap. Defining $\Delta y(s) := y_1(s) - y_2(s)$, we consider an additional energy potential of the form

$$\mathcal{E}_{interaction} = f(\Delta y - 2\delta)^{-2}, \quad [16]$$

where f characterises the strength of the repulsive interaction. While this forms a quite simplified description of interaction energy that neglects non-local interactions and also ceases to be accurate in large deformation, the simplicity enables for quick computation and it is sufficient for comparing energies to determine which deformation branch the buckling will follow.

In particular, we wish to compare the energy in the distinct configurations in which the mantle edges are ‘‘in phase’’ and ‘‘out of phase’’. These configurations are obtained by first computing the preferred buckling shape of the mantle in isolation. The critical buckling mode is determined by the mechanical properties of the mantle and the strength of attachment to the shell edge, characterised by the length of domain and the parameter k (the bending stiffness can be scaled to unity). In particular, we linearise the above equations (neglecting the interaction force) for $|\theta(s)| \ll 1$, leading to a single fourth order equation

$$y''''(s) - \gamma^2 n_x y''(s) + \gamma^4 y(s) = 0,$$

along with boundary conditions

$$y(0) = y'(0) = y(L) = y'(L) = 0.$$

In the system above γ is set to a value just slightly larger than 1 to trigger buckling* and n_x is an unknown compressive stress that serves as an eigenvalue to determine buckling. The system has an infinite but countable set of solutions; the buckling mode is determined by the solution corresponding to the smallest (in magnitude) value of n_x .

The buckling forms a bifurcation from the trivial straight solution with two solution branches of equal energy that are mirror images of each other, e.g. if $(s, y(s))$ describes the buckled shape on one solution branch, then $(s, -y(s))$ is a separate but energy-equivalent solution branch. Denoting the two valves with subscript 1 and 2, the in phase solution is constructed by taking the initial solutions

$$\mathbf{r}_1 = (s, y(s) + \delta), \quad \mathbf{r}_2 = (s, y(s) - \delta),$$

Thus, both mantle edges have the same shape, with a vertical distance equal to the mantle width between them. For the out of phase solution, we set

$$\mathbf{r}_1 = (s, y(s) + \delta), \quad \mathbf{r}_2 = (s, -y(s) - \delta),$$

so that in this case the two buckled patterns overlap. The repulsive interaction force is then introduced (via numerical continuation) until the out of phase solution is geometrically compatible (defined by the condition $\Delta y > 0$ for $s \in (0, 1)$), and both patterns then evolve by further increasing the growth through the parameter γ . The energy in each configuration consists of the interaction energy as given above as well as a bending energy

$$\mathcal{E}_{bend} = \frac{1}{2} m_i(s)^2$$

and a foundation energy

$$\mathcal{E}_{foundation} = \frac{k}{2} (y_i(s) - (-1)^i \delta)^2,$$

where each energy contribution is integrated over the domain $s \in (0, L)$. Figure 3 in the main text was computed using parameter values $L = 20$, $k = 40$, $\delta = 0.03$, and $f = 0.5$.

*Since the beams are inextensible any growth will induce buckling.

4. A note on computation

The sections above are used to formulate the base shell, the plane of ornamentation, and the ornamentation pattern. With these ingredients, we follow the steps below to simulate a full shell:

1. For given coiling rates we compute the base shell $\mathbf{r}(s, t)$ as given in Eq. (8).
2. For given mechanical stiffness k , we compute the preferred buckling pattern, given by the parameterised curve $(s, y(s))$.
3. We determine the plane of ornamentation for each material point s and development time t . The plane is comprised of two basis vectors: \mathbf{d}_3 , the tangent along the shell edge, and $\hat{\mathbf{v}}$, which characterises how much the plane has been rotated from being antimarginal as described in Section 2. The directions $\mathbf{d}_3, \hat{\mathbf{v}}$ are associated with the x and y axes in the mechanical description.
4. The mechanical pattern is superimposed on the base shell in the plane of ornamentation, scaled both by the dilation factor $\lambda(t)$ (to simulate uniform mantle growth with shell dilation) and the coiling secretion rate b (to simulate the link between secretion and mantle growth). The full valve thus has the parameterisation $\mathbf{R}(s, t) = \mathbf{r}(s, t) + \lambda(t)b\mathbf{y}(s)\hat{\mathbf{v}}(s, t)$.
5. To produce the full shell with closed halves simply requires rotating each shell surface about its hinge (the y axis) by the amount $b \ln(1+t)$. In the final product both shell edges are contained in the x - y plane.

5. Asymmetric coiling and large scale deformation

In this section we consider the impact of a large scale deformation on the coiling geometry for two asymmetrically coiling valves. A schematic is shown in Figure 2. The intuitive idea is that the small scale instability occurs initially but is largely focussed at the thin periostracum, while the centreline of each mantle remains straight and thus the two valves still meet in a single plane. Under the assumption that mantle growth is linked with coiling, for asymmetric coiling the two mantle halves will be growing at different rates. This mismatch induces stress in each mantle that is relieved by a secondary, large scale instability. Following the large scale instability the two valves no longer meet in a single plane.

We first consider the question of how the coiling in each valve might adapt following the large scale deformation. To simplify the argument, we restrict attention to the longitudinal center of each valve (the point $s = 0$ for the half circle $\mathbf{r}_0 = (\cos s, \sin s, 0)$). At $s = 0$ the shell traces out a planar logarithmic spiral (prior to small or large scale instability) with maximum arclength. Further, the notation can be simplified by casting the problem in the complex plane. To do this, we write the two spirals $\mathbf{r}_i(0, t)$, as the complex functions

$$\begin{aligned} z_1(t; \tau) &= (1+t)e^{i(b_1 \ln(1+t) - \phi_1(\tau))} \\ z_2(t; \tau) &= (1+t)e^{-i(b_2 \ln(1+t) - \phi_2(\tau))}. \end{aligned} \quad [17]$$

The expression above is defined for $0 < t < \tau$, i.e. τ is the ‘‘current development time’’. The terms $\phi_i(\tau) = b_i \ln(1+\tau)$ are the rotation angles. In particular, the rotation implies that $\text{Im}z_i(\tau; \tau) = 0$. Note also that $\text{Re}z_1(\tau; \tau) = \text{Re}z_2(\tau; \tau) = (1+\tau)$, so that the ends of both curves meet (this is simply a restating of the coinciding of the two shell edges via the full geometric construction), even with coiling asymmetry $b_1 \neq b_2$. It is this asymmetric case that is of interest, so let us assume that before the large scale deformation we have $b_i = \hat{b}_i$ with \hat{b}_i constant such that $\hat{b}_1 > \hat{b}_2$.

As described in the main text, the large scale deformation locally changes the geometric constraint imposed by the presence of the other valve, and thus the coiling rates must adapt to the changing geometric constraint. We can account for this in the formulation above by imposing $\text{Im}z_i(\tau; \tau) = \hat{y}(\tau)$, where the function $\hat{y}(\tau)$ describes the displacement from the base case (i.e. in the base case $\hat{y}(\tau) = 0$ and the two curves meet along the x -axis). For given \hat{y} , the coiling rates b_i will vary in order to satisfy $\text{Im}z_i(\tau; \tau) = \hat{y}(\tau)$. From this we obtain

$$\begin{aligned} b_1(t) &= \left(\arcsin \frac{\hat{y}}{1+t} + \hat{b}_1 \ln(1+t) \right) / \ln(1+t) \\ b_2(t) &= \left(\hat{b}_2 \ln(1+t) - \arcsin \frac{\hat{y}}{1+t} \right) / \ln(1+t). \end{aligned} \quad [18]$$

Observe that $b_i = \hat{b}_i$ when $\hat{y} = 0$. These formulas provide a rule for how the coiling updates locally when the plane between the two valves is deformed. Thus, for given \hat{y} , the functions z_i are modified to

$$\begin{aligned} z_1(t; \tau) &= (1+t)e^{i(b_1(t) \ln(1+t) - \phi_1(\tau))} \\ z_2(t; \tau) &= (1+t)e^{-i(b_2(t) \ln(1+t) - \phi_2(\tau))}. \end{aligned} \quad [19]$$

with $b_i(t)$ given by Eq. (18) (and thus no longer describe logarithmic spirals). It is important to note that the rotation functions are unchanged: $\phi_i(\tau) = \hat{b}_i \ln(1+\tau)$. This reflects the fact that the deformation \hat{y} is *local*, i.e. will be different for different points along the shell edge, while the rotation of the hinge is a *global* property. As some points will deform up ($\hat{y} > 0$ say) and others down, the rotation will most naturally follow that in the base case.

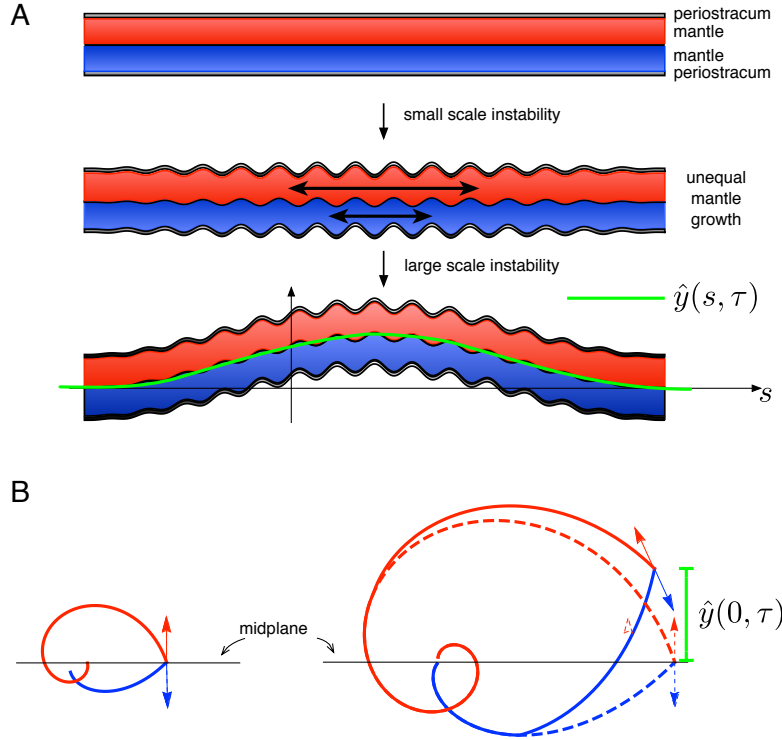


Fig. 2. A. Schematic of the small- and large-scale patterns. The shell secreting mantle-periostracum system forms a bilayer with thick and soft mantle and thin and stiff periostracum. In this schematic, the red mantle corresponds to the valve with higher coiling rate. The small-scale instability appears initially as a wrinkling pattern primarily impacting the periostracum (but nevertheless communicated to both valves). Since the red mantle is assumed to be growing at a higher rate in correspondence with increased coiling, a compressive stress is developed that is relieved by buckling of the entire mantle-periostracum system. As this is significantly thicker than the periostracum the buckling is of much lower mode than the small-scale pattern. The deformation function \hat{y} follows the average of the two mantles. In B, we follow the longitudinal mid point of each shell to show how the coiling adapts to the large scale pattern. The large-scale pattern has not yet occurred in the spirals on the left, so that both shells still meet in a single plane. At right, once the large-scale instability occurs the shells no longer meet in a single plane. In this example, the point $s = 0$ deforms toward the red mantle, i.e. $\hat{y}(0, \tau) > 0$; accordingly the red mantle must decrease its coiling rate and the blue mantle must increase (as seen by comparison with the dashed curves, which show the case with no large-scale deformation). The arrows indicate the direction of plane of ornamentation. In response to the large-scale pattern the plane has been tilted compared to the vertical plane in the base case, but the plane for the two valves still perfectly aligns.

As a first check on whether interlocking can be maintained, we ask whether the two ends of the curve still meet. This is not automatic, as we have only imposed that the imaginary parts are equal at $t = \tau$. A simple computation gives that

$$\text{Re}z_1(\tau; \tau) = \sqrt{(1 + \tau)^2 - \hat{y}(\tau)^2} = \text{Re}z_2(\tau; \tau).$$

Thus, if coiling is forced to adapt to a given y -value, it does so such that the x -values still agree.

A. Tilt with large scale deformation. The calculations above show that if the coiling in each valve adapts to a local deformation of the mantle tissue, the ends of the curves will still meet. To extrapolate this idea from two spiral curves to two bivalve surfaces, we suppose that a deformation function is given both as a function of development time and material point, i.e. we take $\hat{y} = \hat{y}(s, \tau)$. This function would formally come as the output of a mechanical model (see Section 6); for present we take this function as a given. Then, $\hat{y}(s, \tau)$ can be input into formulas Eq. (18) so that the variation in coiling is extrapolated to space and time, $b_i = b_i(s, t)$. We then simulate the full shell by inserting the form $b_i(s, t)$ into the geometric construction of Section 1, in particular we change the constant b to the function $b_i(s, t)$ in the analytical shell parameterisation Eq. (8)[†]. At this point, we have a parameterization for a smooth bivalved shell with large scale deformation imposed. At all times, the edges of the shell perfectly meet, but no longer lie in a single plane. It remains to impose the small scale deformation on top. Technically this is working in the wrong order: as stated in the main text, in brachiopods the small scale deformation appears first; nevertheless from the geometric point of view the patterns are interchangeable. Moreover, \hat{y} will have the form $\hat{y} = f(s, \tau)H(\tau - \tau^*)$ where $H(x)$ is the Heaviside function, defined to be 0 for $x < 0$. Here τ^* represents the development time at which the large scale instability occurs. Since the small scale instability is imposed at $\tau = 0$, in our construction the small scale pattern does indeed appear first.

[†]This is not technically correct. Once b is dependent on s and t , the analytical construction derived in Section 1 ceases to work. However this model simplification nevertheless produces a shell with the desired characteristics of adaptive coiling to large scale deformation, whereas the full model would be analytically untractable.

To determine whether interlocking is maintained once the small scale pattern is included, we proceed with the same logical argument as in the symmetric case described in the main text and with computations outlined in Section 2 above. The important question is whether the plane of ornamentation agrees (*pointwise*) between the two valves. The conceptual approach is identical to what we have outlined in Section 2: we define a unit vector $\hat{\mathbf{v}}$ which is perpendicular to the tangent along the shell edge (\mathbf{d}_3) rotated by an amount such that if the surface is moved by an amount λ in the positive $\hat{\mathbf{v}}$ direction, and separately moved by an amount λ in the negative $\hat{\mathbf{v}}$ direction, the arclengths are equal.

The calculation itself is more involved due to the increased complexity in base geometry, but is provided below for completeness. The result is as in the base case: a nonlinear ODE in time is derived for $\theta_i(s, t)$, the angle of tilt of the plane of ornamentation from the ‘true antimarginal’ plane; with $i = 1, 2$ for the two asymmetric valves. Once θ_i is computed, the degree of alignment between the planes of ornamentation of the two valves, denoted \mathcal{A} , is defined as

$$\mathcal{A}(s, t) = R(\phi_1(t), \mathbf{e}_y)\hat{\mathbf{v}}_1(s, t) \cdot R(-\phi_2(t), \mathbf{e}_y)\hat{\mathbf{v}}_2,$$

where the rotation matrices R are needed to account for the global hinge rotation for each valve. As before, $\mathcal{A} = 1$ if the planes of ornamentation perfectly agree.

Examples of the surface $\mathcal{A}(s, t)$ for both low and high asymmetry are provided in Figure 3. While not quite as perfect as in the base case, the alignment is still quite good throughout development, perhaps even remarkably so considering the significant geometric variations imposed.

The adapted coiling and computed tilt is shown on the curves at the longitudinal center in Figure 2B. The spirals on the left are prior to the large scale deformation; the red curve has increased coiling rate compared to the shallower blue curve, but both curves meet at the same point on the midplane. Following deformation, the curves no longer meet at the midplane (as in the base case, shown in dashed curves), but at the point with $\hat{y}(0, \tau) > 0$. The computed angle of plane of ornamentation is indicated by the arrows; while the plane has been tilted (locally) compared to the base case, a perfect correspondence of angle is maintained between the two curves.

Computing plane of ornamentation and producing full shell With $b = b(s, t)$ (subscript i dropped here for convenience), we work in the orthogonal (but not orthonormal) basis

$$\mathbf{d}_1 = \begin{pmatrix} \cos s \cos(\beta(s, t)) \\ \sin s \\ \cos s \sin(\beta(s, t)) \end{pmatrix}, \quad \mathbf{d}_2 = \begin{pmatrix} -\cos s \sin(\beta(s, t)) \\ 0 \\ \cos s \cos(\beta(s, t)) \end{pmatrix}, \quad \mathbf{d}_3 = \begin{pmatrix} -\sin s \cos(\beta(s, t)) \\ \cos s \\ -\sin s \sin(\beta(s, t)) \end{pmatrix}, \quad [20]$$

where $\beta(s, t) := b(s, t) \ln(1 + t)$. In this basis the shell surface with large-scale pattern but prior to small-scale ornamentation (and without any global rotation) satisfies $\mathbf{r} = (1 + t)\mathbf{d}_1$ from which we compute the temporal and spatial tangents

$$\dot{\mathbf{r}} = \mathbf{d}_1 + c_1(s, t)\mathbf{d}_2, \quad \mathbf{r}' = (1 + t)\mathbf{d}_3 + c_2(s, t)\mathbf{d}_2,$$

where $c_1 = b + (1 + t)\dot{b} \ln(1 + t)$, $c_2 = (1 + t)b' \ln(1 + t)$. We determine the plane of ornamentation by rotating the unit vector $\dot{\mathbf{r}}/|\dot{\mathbf{r}}|$ about $\mathbf{r}'/|\mathbf{r}'|$ by an angle $\theta(s, t)$ to be determined. These can be written in the local basis as

$$\mathbf{u} := \frac{\dot{\mathbf{r}}}{|\dot{\mathbf{r}}|} = \frac{1}{\sqrt{c_2^2 + (1 + t)^2}} \begin{pmatrix} 0 \\ c_2 \\ 1 + t \end{pmatrix}, \quad \mathbf{w} := \frac{\mathbf{r}'}{|\mathbf{r}'|} = \frac{1}{\sqrt{1 + c_1^2}} \begin{pmatrix} 1 \\ c_1 \\ 0 \end{pmatrix}. \quad [21]$$

The plane of ornamentation is then the \mathbf{u} - \mathbf{v} plane where $\mathbf{v} = R(\theta, \mathbf{u})\mathbf{w}$, R being a rotation matrix about \mathbf{u} . By the same computation as before, the equation governing equal arclengths at the peaks and valleys of the small pattern is

$$\dot{\mathbf{r}} \cdot (\mathbf{v} + (1 + t)\dot{\mathbf{v}}) = 0. \quad [22]$$

Expanding this expression and using the orthogonality of the basis, we can obtain an explicit ODE for θ :

$$(1 + t)B_1\dot{\theta} = - [v_1 + \cos^2(s)c_1v_2 + (1 + t)(\mathbf{d}_1 + c_1\mathbf{d}_2)(v_1\dot{\mathbf{d}}_1 + v_2\dot{\mathbf{d}}_2 + v_3\dot{\mathbf{d}}_3) + (1 + t)B_2] \quad [23]$$

where B_1 and B_2 are the coefficients of $\dot{\theta}$ and θ , respectively, in the expression

$$\dot{v}_1 + c_1 \cos^2(s)c_1\dot{v}_2.$$

In the above we are decomposing $\mathbf{v} = v_1\mathbf{d}_1 + v_2\mathbf{d}_2 + v_3\mathbf{d}_3$, where computationally each v_i is obtained by taking the i th component of $R(\theta, \mathbf{u})\mathbf{w}$. To avoid overflow in algebraic complexity, our approach was to define the ODE Eq. (23) generically, i.e. before inputting a specific form of $\hat{y}(s, t)$ that feeds into the specific form of $b(s, t)$ given by Eq. (18) and therefore into all of the component functions c_i , B_i , etc. The resulting ODE, once specific forms were input, could then be integrated numerically without issue. The resulting complete valve, with both small and large scale pattern, is then defined by

$$\mathbf{r}_{\text{full}} = \mathbf{r} + (1 + t)y(s)(v_1\mathbf{d}_1 + v_2\mathbf{d}_2 + v_3\mathbf{d}_3), \quad [24]$$

where the small scale pattern is built into the function $y(s)$ as above, the factor $(1 + t)$ accounts for the scaling of the small-scale pattern with growth, while the large scale pattern is built into the v_i as well as the adapted basis. Both valves would be produced in the same basic manner, with appropriate reflections and rotations to bring the two halves together.

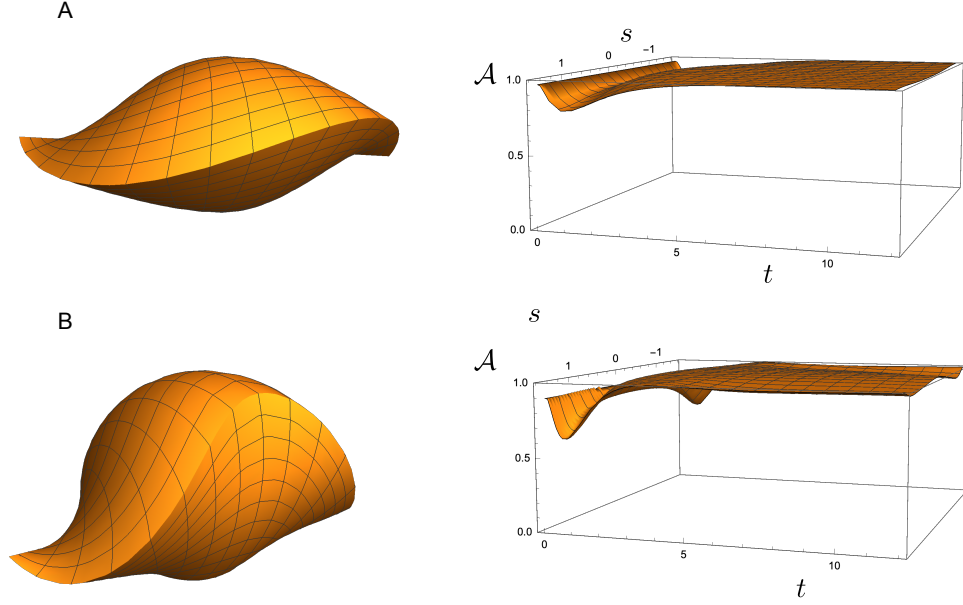


Fig. 3. Alignment measure of plane of ornamentation for a shell with low asymmetry (A) and a shell with high asymmetry (B). The simulated shells prior to small-scale ornamentation are shown at left (in A we have taken $b_2 = 1$, $b_1 = 1.7$, in B the coiling rates are $b_2 = 1$, $b_1 = 3$), the surface of alignment measure \mathcal{A} is shown at right. Perfect alignment again corresponds to $\mathcal{A} = 1$.

6. Mechanical model for large-scale instability

In this section we outline the mechanical model for the large-scale instability. Conceptually, the idea is similar to the small-scale instability calculation of Section 3, in that we model the process as two growing elastic beams that are in physical contact[‡]. Hence our starting point is again the balance of force and moment for two growing elastic beams with an interaction force, however with a few key differences. For one, as we are testing the hypothesis that the large-scale pattern emerges due to a differential growth between the two valves, we must incorporate non-equal growth. Connected to this, we drop the inextensibility assumption. Since the large-scale pattern involves (in our modelling view) the deformation of the entire mantle-periostracum structure (Fig 2A), which is composed largely of the thick and soft mantle, we suppose that in a rod setting the material may support extension and compression. This would seem to be a reasonable choice; it also a necessary ingredient for the large scale instability to not occur immediately: with extensibility and unequal growth, the system will remain in the trivial unbuckled state and an increasing build-up stress until a buckling threshold is reached. If the beams were taken to be extensible, any difference in growth could only be relieved by a deformation from the flat state.

Letting $i = 1, 2$ for the two mantle/periostracum structures (hereafter referred to simply as the mantles for convenience), we have the geometric relations

$$x'_i(s) = \alpha_i \gamma_i \cos \theta_i(s), \quad y'_i(s) = \alpha_i \gamma_i \sin \theta_i(s), \quad [25]$$

where again s is a Lagrangian material parameter, $\theta_i(s)$ is the angle between the tangent to the curve and the x -axis, and $\alpha_i(s)$ describes the stretching (or compression) of the beam (in an inextensible model $\alpha \equiv 1$ by construction). As before γ_i characterises the growth of each mantle. The objective here is to impose a growth rule that links to a difference in coiling rates b_i . For simplicity, we consider the rule

$$\gamma_i(t) = 1 + b_i t.$$

In this way, for given coiling rates the development time t forms the bifurcation parameter from the initial flat state $y_i(s) \equiv 0$.

As before, balance of force and moment read

$$\mathbf{n}'_i(s) + \mathbf{f}_i = 0, \quad m'_i(s) = \gamma_i n_{i_x} \sin \theta_i - \gamma_i n_{i_y} \cos \theta_i, \quad [26]$$

along with the constitutive relation $m_i = E_b \theta'_i(s) / \gamma_i$. For an extensible beam, we have an additional constitutive law relating axial stress to stretch:

$$n_{x_i} \cos \theta_i + n_{y_i} \sin \theta_i = E_s (\alpha_i - 1),$$

[‡]Note that at the level of mechanics we are not coupling the small scale and large scale pattern, as this would introduce unnecessary complexity. Such a model would require a full 3D description of the multilayer mantle/periostracum structure that would likely require highly computational tools such as finite elements to resolve. Such complexity is not relevant to understanding the trends we are considering here, and thus we leave such modelling for future work.

where $E_s = EA$ is the stretching stiffness, with A the cross-sectional area.

As in the small-scale pattern, we wish to impose a form of contact force \mathbf{f}_i that forbids the center lines to cross but allows some deformation. In Section 3, the main objective was to compute buckling mode and determine which deformation path had lowest energy, for which the simple form of contact potential Eq. (16) sufficed. Here the task is more challenging: to compare with data on morphological features, we need to compute the bifurcation point and also follow the (nonlinear) solution branch following bifurcation in order to predict large scale relative amplitude as a function of coiling asymmetry. For this we impose a more detailed form of contact energy potential

$$\mathcal{E}_{interaction} = f \left[\frac{1}{m} \left(\frac{\delta}{\Delta y} \right)^m - \frac{1}{n} \left(\frac{\delta}{\Delta y} \right)^n \right],$$

where again $\Delta y(s) := y_1(s) - y_2(s)$, f is a constant characterises the strength of interaction, and $m > n$ are integers. This form of interaction potential has the form of a Leonard-Jones potential, with a minimum at $\Delta y = \delta$, divergence as $\Delta y \rightarrow 0$, and a decaying energy for $\Delta y \gg \delta$, with the rate of divergence/decay determined by the constants m and n [§]. The minimum at $\Delta y = \delta$ corresponds to repulsion when the mantles come together and a slight attractive force when the two mantles are pulled apart; the latter models mild adhesion of the mantle surfaces due for instance to surface tension effects.

The system is closed by imposing clamped boundary conditions. Here, a crucial aspect is growth of the domain: whether or not buckling occurs depends on the growth of the mantles relative to the expanding length of the shell edge. To test the link between asymmetry and secondary pattern, we suppose that the domain growth exactly matches the growth of mantle 2. For simplicity we fix coiling rate $b_2 = 1$ so that mantle 2 has reference length $L_0(1 + t)$, where L_0 is the initial length, and we impose a matching length of domain $L(t) = L_0(1 + t)$. The boundary conditions are then

$$y_i(0) = y_i(L(t)) = (-1)^{i+1} \frac{\delta}{2}, \quad \theta_i(0) = \theta_i(L(t)) = 0.$$

With this construction, if the coiling is symmetric, i.e. if $b_1 = 1$ also, no stress is induced and a bifurcation from the flat state will never occur. The procedure then is to fix $b_1 > 1$ and seek the critical time t^* at which the first bifurcation occurs, and then follow that solution branch. This was solved using the numerical continuation software AUTO-07p (2).

The orange squares in the main text Fig 7B were obtained by computing the solution branch as described above until the maximum amplitude of the deformed shape, $A(t) := \max_{s \in (0, L(t))} |y_1(s)|$, reached a fixed value A^* ; that is we integrate the system forward until time t^* at which $A(t^*) = A^*$. The relative amplitude is then defined as the ratio $A^*/L(t^*) = A^*/(L_0(1+t^*))$. In producing the points in main text Fig 7B we used the parameter values $L_0 = \pi$, $k = 0.05$, $\delta = 0.3$, and $A^* = 1.5$. These values generate a low buckling mode in correspondence with the observed pattern on shells; and the choice of A^* was made based on the visual appearance of the pattern. Alternative choices make a quantitative difference but do not change the general trend.

In Figure 4 we plot the bifurcation diagrams of $A(L(t))$ against $L(t)$ for several values of b_1 . It is evident that as the asymmetry is increased, the instability occurs earlier, i.e. at a shorter length, and thus the relative amplitude is higher. Also included in Figure 4 is the profile of the two mantles at the marked points. While the model as described captures well the trend of increasing relative amplitude with increasing asymmetry, there are a few features predicted by the model that do not (necessarily) correspond to what is observed in brachiopod shells. For one, at the lower values of asymmetry, the buckling mode is odd (mode 2) whereas at higher values it is even (mode 1). This is because the domain length has increased significantly before bifurcation in the low asymmetry case, and hence a higher mode is triggered. While both even and odd modes are observed in shells, we did not access the specimens required to test quantitatively a correspondence between low asymmetry and odd mode pattern. It would require indeed a collection of specimens of the same species displaying an important intraspecific variation and specimens with both odd and even mode. We thus leave this question as future work. It is also worth noting that with a small change in parameters in the mechanical model, for instance increasing k , the trend of even versus odd mode could be reversed: if k (a parameter that we cannot ascertain with any certainty) were such that the early buckling high asymmetry pattern were an odd mode, then the later buckling low asymmetry would tend to be again one mode higher, which would be an even mode.

More concerning in terms of comparing with observations in shells is the fact that with high enough asymmetry the bifurcation branch suffers a discontinuity and hysteresis loop. For instance, in the case $b_1 = 5$, if the bifurcation branch is followed beyond $A = 2$, the solution branch folds back towards decreasing L and then folds again at a later point. Also, for $b_1 > 5$ the bifurcation is subcritical and so a discontinuous jump would appear immediately at the point of buckling. At the point of the first fold, since L is only ever increasing, the solution would discontinuously jump to the higher point of the branch – however, this upper branch corresponds to a separation of the two mantles[¶]. Mechanically, this is not surprising: for large asymmetry the growth in mantle 1 is much higher than in mantle 2, they only deform together for a limited time before jumping to a separated state where mantle 1 relieves compression through an increased arclength compared to mantle 2. This feature is highly sensitive to parameter values (see for instance the complex boundary between subcritical and supercritical bifurcation in a related system (3)), so it is difficult to ascertain when this would be predicted. Nevertheless, such a feature is never observed in shells, which suggests that the simplified model of constant unequal growth *for all time* is invalid. This does not negate the mechanical hypothesis but merely suggests that the situation involves a more complex growth process likely including

[§]Results produced here used $m = 4$, $n = 3$, and $f = 1$ alternative choices do not qualitatively change results but do impact on numerical stability.

[¶]In computing the relative amplitude this discontinuity was irrelevant as the value A^* was reached before the jump discontinuity in all cases.

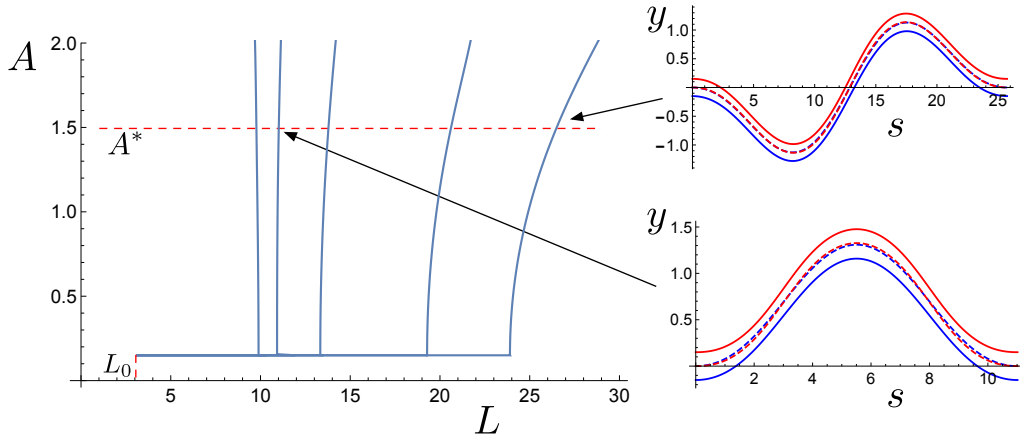


Fig. 4. Bifurcation diagram plotting amplitude $A = \max_{s \in (0, L(t))} |y_1(s)|$ against the growing domain length $L = L_0(1 + t)$. From left to right, the bifurcation branches correspond to $b_1 = 5, 4, 3, 2, 1.7$. Plots of the two mantles are included at the points indicated by the arrows.

feedback. Indeed, the assumption that $\gamma_i = 1 + b_i t$ with each b_i constant is overly simplified. Following Section 5, we could adapt the growth following the rule for coiling adaptation as given in equations Eq. (18). In this way, once buckling occurred, growth in each mantle would locally change based on the deformation at each point. Considering an even mode deformation, if the middle point deformed toward the higher accreting mantle 1 (see Subsection A below), then following deformation the net growth would decrease in mantle 1 and increase in mantle 2, thereby potentially relieving the stress without the need to lose contact. However, implementing such a rule is more challenging, as the growth would be nonuniform and would have to be updated at each time step; this combined with the nonlinearities already present in the system make such a computation intractable within the AUTO-07p framework we have implemented and goes beyond the scope of this manuscript.

A. On the preference for buckling direction. In the mechanical model, the bifurcation consists of two branches. For an odd mode, the two branches are reflections of each other about the x -axis. In the case of an even mode buckling, in one branch the midpoint deforms up, i.e. towards mantle 1 with $y_i(L/2) > 0$, and in the other branch the midpoint deforms down towards mantle 2. In the mechanical model as we have derived it, each of these branches is energetically equivalent and thus there is no preference for which branch the deformation follows[†]. In brachiopods, this equivalence *is* observed in the case of odd mode patterns: left and right deformations are found with equal frequency (see discussion in main text Section 3.C). With even modes, however, it is always the case in brachiopod that the midpoint of the large scale pattern deforms towards the dorsal side, which is the side with higher coiling rate (mantle 1 in our framework). Mechanically, a perfect pitchfork bifurcation is never physically observed; in reality, unavoidable imperfections and/or noise in the system will preference buckling to one side or the other (4). The fact that the trend is *always* to the dorsal side in the even mode case implies that the buckling direction is not driven by noise or small imperfections (which could vary from shell to shell), but is due to a fundamental feature. A natural candidate is the asymmetry itself. Since the dorsal side is coiling at a higher rate, it is accreting at a higher rate. Inherent in our coiling adaptation model is the notion that the mantle is capable of changing the accretion rate. Considering the midpoint, where the deformation is highest, buckling toward mantle 2 would require an increase in accretion of the already higher accreting mantle 1 and a decrease in accretion of the lower accreting mantle 2. It may be easier, on the other hand, for mantle 1 to decrease its high accretion and mantle 2 to increase its low accretion, which would correspond to buckling in the direction of mantle 1. In other words, the accretive rates of the two mantles are brought closer together by a buckling toward the dorsal side of mantle 1; and this may be energetically favorable (biochemically if not mechanically). Testing this hypothesis is beyond the scope of this work; nevertheless it is worthwhile to note that while this mechanism would force the buckling of even modes towards the higher coiling side, it would not impact the odd mode preference. In the odd modes, there is a flip symmetry along the shell edge so that an increase in accretion on the left side means a decrease in accretion on the right side; hence the buckling would be predicted to have no preference.

B. Simulated shells in main text Figure 7B. In producing the simulated shells appearing in Figure 7B in the main text, we have taken the large scale pattern corresponding to the bifurcation branches $b_1 = 1.7$ and $b_1 = 3$ and used these to produce the surface $\hat{y}(s, \tau)$ as described in Section 5 – this includes the trivial flat solution prior to buckling, and thus naturally has the form $\hat{y} = f(s, \tau)H(\tau - \tau^*)$ where τ^* is the buckling time. This solution was then fed into the geometric framework for computing the plane of ornamentation for each valve, and the small-scale pattern was superimposed as output from the mechanical model of

[†] Due to the unequal growth, the two branches in the even mode case are not mirror images; nevertheless we find that the energy is equal in each branch

Section 3 with the parameters $L_0 = 20$, $k = 500$ (equivalent to the parameters used in the morphospace of main text Fig 6)**.

7. Data collection

The data in Figure 7B of the main text was produced by importing a side and front profile picture of each shell into Mathematica and overlaying logarithmic spirals of the form $r(\theta) = ae^{\beta\theta}$ on the side profile and sinusoids on the front profile (as shown in main text Fig7A). We then varied the parameters of the logarithmic spiral – the scale factor a and the tightness of spiral b – and also added a rotation and translation to make the spiral align with the shell profile. Given the self-similar form of a logarithmic spiral, the scale factor is irrelevant, it is only the quantity b that is extracted to determine the coiling rate. The objective was to match the shape of the mid-longitudinal point of the shell (the spiral corresponding to $s = 0$ in our modelling framework), which by symmetry is assumed to be the edge of the shell in the photo. Here it is important to note that as we seek to extract the baseline coiling rate, we only attempted to fit the portion of the shell *prior* to large-scale deformation. The parameters were chosen by best visual fit; a similar exercise was performed for the front view sinusoids. To avoid confirmation bias, all shells were fit in sequence and prior to plotting any data. We compute a Spearman’s rank correlation coefficient of 0.671, and a p-Value less than 0.0001, indicating a moderate to high correlation, though we note that due to inherent sources of measurement error the data is better interpreted as indicative of a qualitative trend than a quantitative rule.

The extracted parameters b_1 , b_2 , and A/L for each shell, as well as images of the overlaid curves, are given in Tables 1-4. Also needed to compare with the model is a map between the spirals $r(\theta) = ae^{\beta\theta}$ and the coiling rate b in the geometrical construction. Noting that at the point $s = 0$ the geometric construction produces the curve (see equation Eq. (17)) $x = (1 + t) \cos(b \ln(1 + t))$, $y = (1 + t) \sin(b \ln(1 + t))$, this can be written as a polar curve $r(\theta) = e^{\beta\theta}$ by making the substitution $\theta = b \ln(1 + t)$, from which we see the relation $\beta = 1/b$.

1. Moulton DE, Goriely A (2014) Surface growth kinematics via local curve evolution. *Journal of mathematical biology* 68(1-2):81–108.
2. Doedel EJ, et al. (2007) Auto-07p: Continuation and bifurcation software for ordinary differential equations.
3. Almet AA, Byrne HM, Maini PK, Moulton DE (2018) Post-buckling behaviour of a growing elastic rod. *Journal of mathematical biology* 78(3):1–38.
4. Hutchinson JW, Koiter WT (1970) Postbuckling theory. *Appl. Mech. Rev* 23(12):1353–1366.

** Following this protocol produced a too-rapid increase in amplitude of large-scale pattern, i.e. visually the large scale deformation appeared too sharp on the scale of the shell; hence in imposing the large-scale pattern on the shell we first rescaled the time parameter t in the large-scale model as $t = \hat{t}/4$ to stretch out the pattern relative to the shell. This rescaling would correspond to a dampening of the rate of coiling on mantle growth; e.g. instead of taking $\gamma_i = 1 + b_i t$ we would have $\gamma_i = 1 + \beta b_i t$ with $\beta < 1$. Alternatively, a change in parameters L_0 and k could also have the effect of decreasing the gradient of amplitude increase of the bifurcation curves(3); but as stated we do not have good access to these parameters.

 <p>$b_1=0.41, b_2=0.85, A/L=0.066$</p>	 <p>$b_1=0.357, b_2=0.584, A/L=0.049$</p>	 <p>$b_1=0.438, b_2=0.826, A/L=0.053$</p>
 <p>$b_1=0.454, b_2=1.252, A/L=0.051$</p>	 <p>$b_1=0.109, b_2=1.076, A/L=0.215$</p>	 <p>$b_1=0.206, b_2=0.816, A/L=0.066$</p>
 <p>$b_1=0.0916, b_2=0.816, A/L=0.166$</p>	 <p>$b_1=0.1206, b_2=0.904, A/L=0.119$</p>	 <p>$b_1=0.1656, b_2=0.974, A/L=0.101$</p>
 <p>$b_1=0.1688, b_2=1.048, A/L=0.148$</p>	 <p>$b_1=0.1946, b_2=1.08, A/L=0.12$</p>	 <p>$b_1=0.1828, b_2=0.89, A/L=0.113$</p>
 <p>$b_1=0.166, b_2=1.458, A/L=0.17$</p>	 <p>$b_1=0.1322, b_2=0.586, A/L=0.205$</p>	 <p>$b_1=0.1222, b_2=0.61, A/L=0.128$</p>
 <p>$b_1=0.196, b_2=0.874, A/L=0.126$</p>	 <p>$b_1=0.208, b_2=1.092, A/L=0.104$</p>	 <p>$b_1=0.103, b_2=1.41, A/L=0.129$</p>
 <p>$b_1=0.103, b_2=0.684, A/L=0.141$</p>	 <p>$b_1=0.523, b_2=0.806, A/L=0.06$</p>	 <p>$b_1=0.18, b_2=0.672, A/L=0.138$</p>
 <p>$b_1=0.158, b_2=0.832, A/L=0.116$</p>	 <p>$b_1=0.697, b_2=0.792, A/L=0.061$</p>	 <p>$b_1=0.141, b_2=0.912, A/L=0.16$</p>

Table 1. Extracted parameters and overlaid curves for *Burmihynchia thierachensis*, part 1.

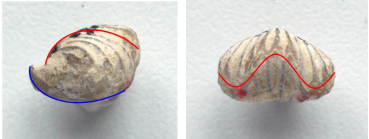
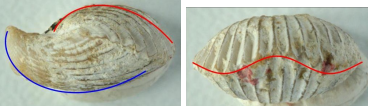
 <p>$b_1=0.101, b_2=0.992, A/L=0.134$</p>	 <p>$b_1=0.241, b_2=0.79, A/L=0.145$</p>	 <p>$b_1=0.199, b_2=0.552, A/L=0.155$</p>
 <p>$b_1=0.112, b_2=0.826, A/L=0.154$</p>	 <p>$b_1=0.027, b_2=0.582, A/L=0.145$</p>	 <p>$b_1=0.433, b_2=0.582, A/L=0.065$</p>
 <p>$b_1=0.278, b_2=0.81, A/L=0.086$</p>	 <p>$b_1=0.178, b_2=0.65, A/L=0.13$</p>	 <p>$b_1=0.054, b_2=0.756, A/L=0.187$</p>
 <p>$b_1=0.245, b_2=0.966, A/L=0.148$</p>	 <p>$b_1=0.469, b_2=0.966, A/L=0.092$</p>	 <p>$b_1=0.311, b_2=0.966, A/L=0.071$</p>
 <p>$b_1=0.416, b_2=0.966, A/L=0.07$</p>	 <p>$b_1=0.416, b_2=1.028, A/L=0.144$</p>	 <p>$b_1=0.416, b_2=1.07, A/L=0.093$</p>
 <p>$b_1=0.093, b_2=1.07, A/L=0.145$</p>	 <p>$b_1=0.085, b_2=1.07, A/L=0.12$</p>	 <p>$b_1=0.085, b_2=1.07, A/L=0.191$</p>
 <p>$b_1=0.634, b_2=1.68, A/L=0.105$</p>	 <p>$b_1=0.686, b_2=0.78, A/L=0.051$</p>	 <p>$b_1=0.998, b_2=1.218, A/L=0.054$</p>
 <p>$b_1=1.024, b_2=1.218, A/L=0.085$</p>	 <p>$b_1=0.674, b_2=1.218, A/L=0.128$</p>	

Table 2. Extracted parameters and overlaid curves for *Burmirhynchia thierachensis*, part 2.

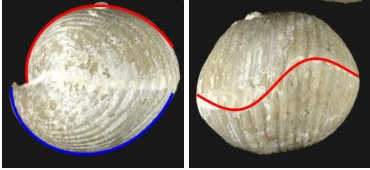

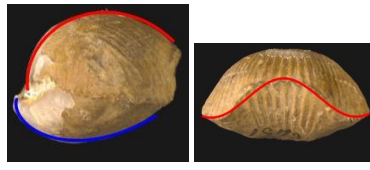
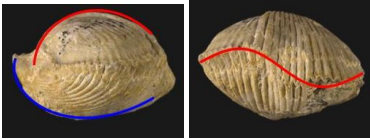
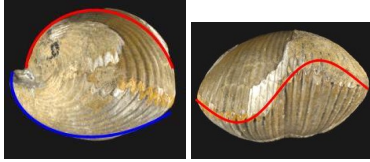
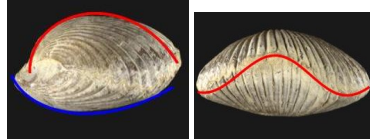

 <p>$b_1=0.41, b_2=0.85, A/L=0.066$ <i>Cyclothyris globata</i></p>	 <p>$b_1=0.354, b_2=0.994, A/L=0.089$ <i>Cyclothyris lamarckiana</i></p>	 <p>$b_1=0.438, b_2=0.826, A/L=0.053$ <i>Cyclothyris lamarckiana</i></p>
 <p>$b_1=0.454, b_2=1.252, A/L=0.051$ <i>Cyclothyris lamarckiana</i></p>	 <p>$b_1=0.109, b_2=1.076, A/L=0.215$ <i>Cyclothyris sp.</i></p>	 <p>$b_1=0.206, b_2=0.816, A/L=0.066$ <i>Cyclothyris sp.</i></p>
 <p>$b_1=0.0916, b_2=0.816, A/L=0.166$ <i>Cyclothyris sp.</i></p>		

Table 3. Extracted parameters and overlaid curves for different species of *Cyclothyris*.

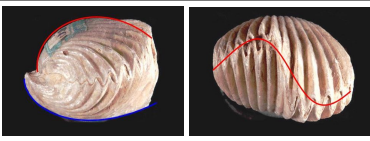
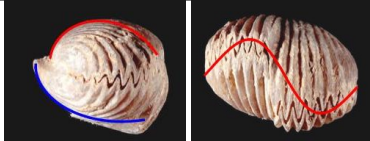
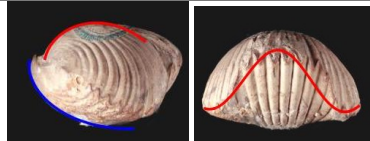
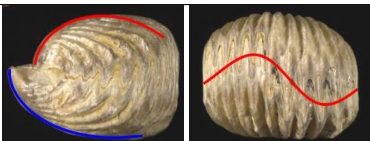
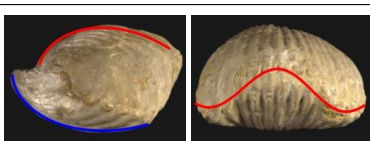
 <p>$b_1=0.432, b_2=1.116, A/L=0.202$</p>	 <p>$b_1=0.348, b_2=1.052, A/L=0.217$</p>	 <p>$b_1=0.432, b_2=1.134, A/L=0.195$</p>
 <p>$b_1=0.502, b_2=1.134, A/L=0.141$</p>	 <p>$b_1=0.856, b_2=1.112, A/L=0.12$</p>	

Table 4. Extracted parameters and overlaid curves for *Torquirhynchia royeriana*.